Materials and Design 186 (2020) 108357

Contents lists available at ScienceDirect

Materials and Design

journal homepage: www.elsevier.com/locate/matdes

Microstructure, defects, and mechanical properties of wire + arc additively manufactured Al—Cu4.3-Mg1.5 alloy

Jianglong Gu [a,b], Minjie Gao [a], Shouliang Yang [a], Jing Bai [c,*], Yuchun Zhai [c], Jialuo Ding [d]

[a] State Key Laboratory of Metastable Materials Science and Technology, Yanshan University, Qinhuangdao 066004, PR China
[b] Hebei Key Laboratory for Optimizing Metal Product Technology and Performance, Yanshan University, Qinhuangdao 066004, PR China
[c] School of Materials Science and Engineering, Northeastern University, Shenyang 110819, PR China
[d] Welding Engineering and Laser Processing Centre, Cranfield University, Bedfordshire MK430AL, UK

HIGHLIGHTS

- The Al—Cu4.3-Mg1.5 alloy was fabricated by wire + arc additive manufacturing.
- The average microhardness reached 161.4 HV for the heat-treated alloy.
- The mean YS and UTS of the heat-treated alloy achieved 399 MPa and 485 MPa.
- Mechanical properties were improved by precipitation strengthening.

GRAPHICAL ABSTRACT

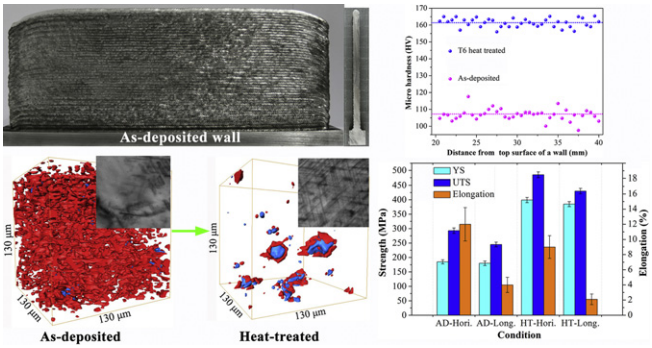

ARTICLE INFO

Article history:
Received 30 August 2019
Received in revised form 24 October 2019
Accepted 12 November 2019
Available online 13 November 2019

Keywords:
Wire + arc additive manufacturing
Al alloy
Al-Cu-Mg
Microstructure
Defect
Mechanical property

ABSTRACT

The wire with a composition of Al—Cu4.3%—Mg1.5% was customized and used to deposit the WAAM alloy with the power source of cold metal transfer. The microstructure, defect, and mechanical properties of the as-deposited and heat-treated WAAM alloys were studied. Key findings demonstrated that the microstructure of the as-deposited alloy was characterized by a hierarchical distribution of dendrites, equiaxed grains, and a slight number of columnar grains. The volume fraction of the network-like scattered coarse particles of second phases θ + S reduced by 95% after the T6 heat treatment. With an average microhardness of 161.4 HV, the mean yield strength and ultimate tensile strength of the WAAM alloy increased by 116% and 66% achieving 399 MPa and 485 MPa in the horizontal direction after heat treatment. The precipitation of a high density of needle-shaped metastable S′ precipitates was responsible for the significantly enhanced mechanical properties. However, this WAAM alloy has exhibited an anisotropic tensile property. A considerable number of sharp-angled defects like linear and chain-like micropores, which generally depress the mechanical properties, were formed in the WAAM alloys.

1. Introduction

Wire + arc additive manufacturing (WAAM) has exhibited significant advantages like greater cost saving of the equipment and feedstock

* Corresponding author.
E-mail address: baij@neuq.edu.cn (J. Bai).

https://doi.org/10.1016/j.matdes.2019.108357

materials, higher deposition rate, and more design flexibility than the traditional subtractive technique [1,2]. The WAAM technique generally adopts robotic manipulator and power sources like gas metal arc welding (GMAW), gas tungsten arc welding (GTAW), plasma, and cold metal transfer (CMT) [3]. In recent years, WAAM has been recognized as an efficient method in producing large-scale aluminum alloy structural parts lengths up to several meters, such as cruciforms, stiffened panels, and wing ribs [4], which are normally used in aircrafts. The mechanical strength, which is particularly crucial for WAAM aluminum alloy components, has attracted considerable attention from the aerospace industry.

However, some works have shown that the difference in heat input do not drastically change the microstructure or mechanical properties of the WAAM material [5,6]. Previous studies on the WAAM aluminum alloys like 2000, 4000, and 5000 series demonstrated that the chemical composition usually has a great influence on their mechanical properties [1,2,4,7]. The WAAM Al—Si5 (4043) aluminum alloy exhibited inferior ultimate tensile strength (UTS), which was 146 MPa by using GTAW as reported by Wang et al. [8]. The UTS and yield strength (YS) of the pulse advanced CMT (CMT-PA) deposited WAAM Al—Cu6.3 (2319) alloy were 260 MPa and 115 MPa, respectively [9]. This result was similar to the alloy with the same composition manufactured by GTAW [10] and the electronic beam [11]. The UTS and YS were 255 MPa and 128 MPa for the GTAW-WAAM Al—Mg5 (5356) alloy [12]. By contrast, the UTS and YS of the GMAW built ternary WAAM Al—Mg4.5—Mn0.7 (5183) alloy and the CMT deposited WAAM Al—Mg4.5—Mn0.9 (5087) alloy were higher, reaching 293 MPa/145 MPa [5] and 291 MPa/142 MPa [13]. With increasing Mg content, the UTS of the WAAM Al—Mg6.3—Mn0.7 (5A06) alloy achieved over 300 MPa by using the variable polarity CMT (CMT-VP) arc as the power source [14].

Generally, the strength of the as-deposited WAAM aluminum alloy cannot meet the requirement from the aerospace industry. Due to the significant increase of dislocation density and refinement of grains, the UTS and YS of the WAAM 2319 and 5087 alloys were increased by 87% and 20% [15], 69% and 18% [13] through a hybrid technique of WAAM + inter-layer rolling. The strength of the heat-treatable WAAM aluminum alloys can be considerably increased through precipitation strengthening by applying post-deposition heat treatment. The UTS and YS of the CMT-PA deposited WAAM 2319 aluminum alloy reached 453 MPa and 315 MPa after T6 (solution treatment + artificial aging) heat treatment [15]. These values exceeded the T6 treated wrought alloy with the same composition.

Aluminum alloys, especially high strength alloys, are prone to defect formation during fusion-based additive manufacturing. The cracking susceptibility and low evaporation temperature of some alloying elements promote solidification cracking and pore formation, which are generally detrimental to the strength [7]. Microalloying is an effective way to decrease cracking susceptibility and increase mechanical properties for aluminum alloys. Currently, most of the research on fusion-based additive manufacturing focused on powder-bed additive manufacturing. For example, researchers found the mixing of Zr powders in 2024 and 7075 alloys could significantly refine grains [16,17]. Comparatively, less research works can be found on the use of grain refiners during WAAM. Due to the inhibition of the oxide layer, alloying powders are difficult to be added into the molten metal. Wang et al. [18] coated Ti powder mixed absolute ethanol on each layer of the WAAM 5356 alloy, and reported the UTS and elongation increased by 20.3–25.9 MPa and 3.1–7.0%, respectively.

Wires of high strength aluminum alloys like 2024, which are heat-treatable and widely used in aerospace and military applications [19], are not supplied in the market until now. Developing of high strength aluminum alloy wire for the WAAM objective is costly since a considerable number of wires with various compositions have to be prepared. This is because the Cu/Mg ratio has a great influence on cracking, microstructure, and mechanical properties of Al-Cu-Mg alloys [20,21]. Gu et al. [22] used a tandem WAAM method by using double wires and pulsed GMAW arc. A series of WAAM Al-Cu-Mg alloys with different compositions were made by controlling the wire feed speeds. They studied the impact of composition, heat input, and microstructure on cracking tendency, obtaining a composition range with minimum susceptibility for the WAAM Al-Cu-Mg alloys. The results are in accordance with the solidification pathway modeling from Scheil analysis by Pickin et al. [23]. Qi et al. [24] deposited Al-Cu-Mg alloys by using the tandem GTAW-WAAM technique. The UTS and YS of the Al—Cu3.6—Mg2.2, Al—Cu4—Mg1.8, and Al—Cu4.4—Mg1.5 were over 280 MPa and 156 MPa in the horizontal (torch travelling) direction. Afterward, this group found the UTS and YS of the tandem GTAW-WAAM Al—Cu4.4—Mg1.5 alloy reached 470 MPa and 374 MPa after the T6 heat treatment [25].

To solve the problems met by the WAAM aluminum alloys, dedicated filler materials should be developed to control the chemical composition, microstructure, and mechanical properties of the deposit [7]. According to the optimized composition from our previous study [22] and the results from Qi et al. [24,25], the wire with a composition of Al—Cu4.3—Mg1.5 was manufactured and served as the single feeding material to deposit walls by using the traditional CMT-WAAM manufacturing system. The microstructure and mechanical properties of the as-deposited and heat-treated WAAM alloys were investigated in this paper.

2. Materials and experiments

WAAM wall samples of the Al—Cu4.3—Mg1.5 alloy were deposited layer by layer with a customized wire with a diameter in 1.2 mm. The commercial wrought 2024-T351 aluminum alloy substrate plate was washed in alkaline water and dried in the air, followed by mechanical cleaning and acetone degreasing. The chemical compositions of the substrate, wire, and WAAM wall were measured by the inductively coupled plasma optical emission spectrometer (ICP-OES) technique (Optima 8300 PerkinElmer) and are listed in Table 1. Aiming to improve the strength and toughness, Mn and Ti were added into the designed alloy. The burning loss of Mg after WAAM deposition was approximately 8%.

The WAAM deposition system was mainly comprised of a Fronius CMT Advanced 4000R power source and an ABB robot (IRB2400). To overcome the low contact angle of the solidified deposit by using the CMT-PA arc mode, a pre-heating of up to 120 °C was adopted to the first layer. The following parameters were set as constant for each layer: wire feed speed of 6 m/min, travel speed of 0.6 m/min, inter-layer cooling time of 2 min, shielding gas flow rate of 25 L/min of pure Ar (99.99%), and contact tip to workpiece distance of 15 mm. The heat input stayed around 120 J/mm during the deposition. Two single-pass multi-layer WAAM walls with a dimension of 380 mm × 110 mm × 6.3 mm were deposited. As shown in Fig. 1a, the torch travelling axis X was defined as the horizontal direction, whilst the deposition direction on Z axis was the vertical direction. The short-transverse that was normal to the torch travelling and deposition directions was defined as Y axis. Half of each wall sliced along the horizontal direction was T6 heat-treated (Fig. 1a). The solution treatment temperature was kept at 498 °C for 1.5 h, followed by cold water quenching. The artificial aging treatment was subsequently carried out at 190 °C for 6 h with a

Table 1
Chemical composition of the as-received substrate and wire, and as-deposited WAAM alloy.

Alloys	Chemical composition (wt%)							
	Cu	Mg	Mn	Ti	Zn	Si	Fe	Al
Substrate 2024-T351	4.27	1.38	0.62	0.10	0.06	0.27	0.30	Bal.
Wire AlCu4.3 Mg1.5	4.36	1.57	0.67	0.15	0.02	0.13	0.11	Bal.
WAAM AlCu4.3 Mg1.5	4.42	1.45	0.68	0.13	0.02	0.08	0.14	Bal.

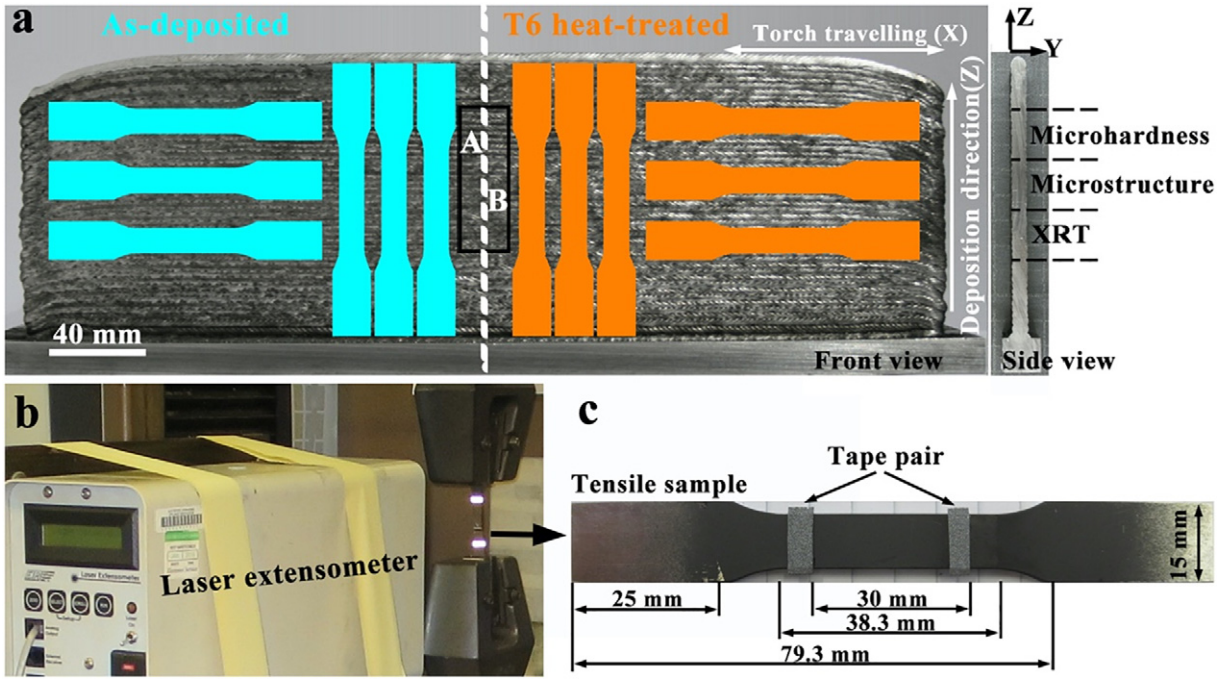

Fig. 1. (a) As-deposited wall of Al—Cu4.3—Mg1.5 alloy; (b) laser extensometer setup; (c) size of dogbone sample for tensile tests.

ramping speed of 100 °C/h from room temperature. All specimens were naturally aged for at least 30 days before testing.

The areas marked as "A" and "B" in Fig. 1a were extracted from the middle of the as-deposited and heat-treated walls, respectively. As shown in the side view, microhardness measurements, microstructure observation, and X-ray tomography (XRT) test were performed on WAAM alloys within the height of 20–40 mm, 40–60 mm, and 60–80 mm from the top, respectively. The microhardness was measured on the as-polished cross-section (YZ plane) along the central line of the vertical direction by using a Vickers microhardness tester Auto-C.A.M.S. of Zwick Roell under a test load of 200 g and 15 s dwell time.

Specimens for metallographic observation were prepared under a standard procedure with grit SiC papers until 4000#, followed by polishing with a 3 μm diamond paste. Colloidal silica suspension (0.04 μm) was applied to final polishing to reach a mirror finish. Keller's reagent (95% water, 2.5% HNO_3, 1.5% HCl, and 1.0% HF) was used for etching. Foils with a diameter of 3 mm for transmission electron microscope (TEM) observation were punched, ground, and subsequently thinned by electropolishing with a twin-jet polisher at −30 °C and 15 V with a solution of 30% nitric acid and 70% methanol. The microstructure and intermetallic phases were characterized by employing the optical microscope (NIKON-Optiphot), TEM (JEOL-JEM-2100F), and field emission scanning electron microscope (FE-SEM, PHILIPS-XL30E) equipped with an energy dispersive spectrometry (EDS, Oxford X-Max 50).

With a height of 15 mm, each specimen for XRT test was ground to a 0.8 mm × 0.8 mm cuboid, followed by ultrasonic wave washing to clean up the abrasive powders. High spatial resolution XRT was performed at the X-ray imaging beamline BL13W1 from the Shanghai Synchrotron Radiation Facility, China. A monochromatic X-ray beam with a photon energy of 20 keV and a transmission ratio of >30% was used. A 2048 × 2048 pixels charge-coupled detector was positioned 15 cm behind the sample to receive the penetrating X-ray. A total of 1200 images containing the contrast information scanned at 180° for each specimen were continuously captured by a CCD camera with a voxel size of 0.65 μm × 0.65 μm × 0.65 μm. The exposure time of each picture was 1 s. Phase recovery, slice reconstruction, image conversion and cutting were performed on projection images by the open-source P3 and P3B software. Avizo was introduced to reconstruct 3D images. To suppress errors originating from image noise, only objects of >5 pixels or the equivalent diameter of >3.25 μm were counted.

Tensile test specimens, three in a set, were cut along both horizontal and vertical directions from each wall as shown on the front view in Fig. 1a. The tensile sample size is shown in Fig. 1c under the standard of ISO 6892-1: 2009. An electromechanical universal testing machine Instron 5500R (30 kN) was employed at room temperature with an initial loading rate of 0.01 mm/min. Strain was measured locally on the specimen using an EIR laser extensometer, which was placed 305 mm ahead of the specimen as shown in Fig. 1b. The gage length between the laser extensometer tape pair was 30 mm as indicated in Fig. 1c. SEM was used to characterize the fracture surface morphology of tensile specimens.

3. Results and discussion

3.1. Microstructure of wire and WAAM alloys

As shown in Fig. 2a, the surface of the customized Al—Cu4.3—Mg1.5 wire was bright and clean. The shallow scratches parallel with the wire drawing direction was caused by the mechanical scraper during the final surface cleaning. This scratch defect generally does not affect the wire feeding during the WAAM deposition. White phase particles with irregular morphology and size were distributed on the α-Al matrix (Fig. 2b). EDS analysis revealed the composition of the bright white A particles, dark white B particles, and rectangular coarse C particles was $Al_{70.34}Cu_{29.66}$, $Al_{61.23}Cu_{21.93}Mg_{16.84}$, $Al_{67.80}Cu_{14.69}Fe_{6.82}Mn_{6.61}Si_{4.08}$. They are θ ($Al_2Cu$), S ($Al_2CuMg$), or Al_6(Fe, Mn, Si) phases, respectively. A ternary eutectic temperature of 507 °C exists in the Al-Cu-Mg alloy according to its ternary phase diagram. The equilibrium phase constitution is α-Al + θ + S. Therefore, the solution treatment temperature was set as 498 °C during the T6 heat treatment for the WAAM alloy.

The cross-section of the as-deposited wall in Fig. 1a suggested stable and excellent formability of the Al—Cu4.3—Mg1.5 alloy wire during the WAAM deposition. Meanwhile, the slight fluctuation of the surface roughness of the wall indicated a high deposition rate and adequate allowance during the subsequent machining for a WAAM part of this alloy. Fig. 3 shows the metallographic images of the as-deposited and heat-treated WAAM Al—Cu4.3—Mg1.5 alloys. As shown in Fig. 3a, the

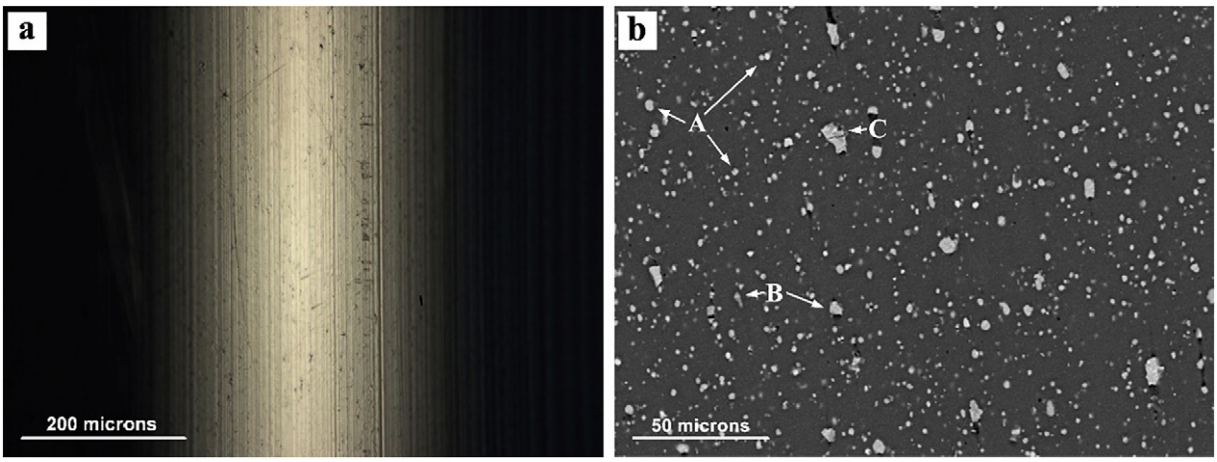

Fig. 2. Wire of Al–Cu4.3–Mg1.5 alloy; (a) macrograph of the surface and (b) distribution of second phase particles in the wire.

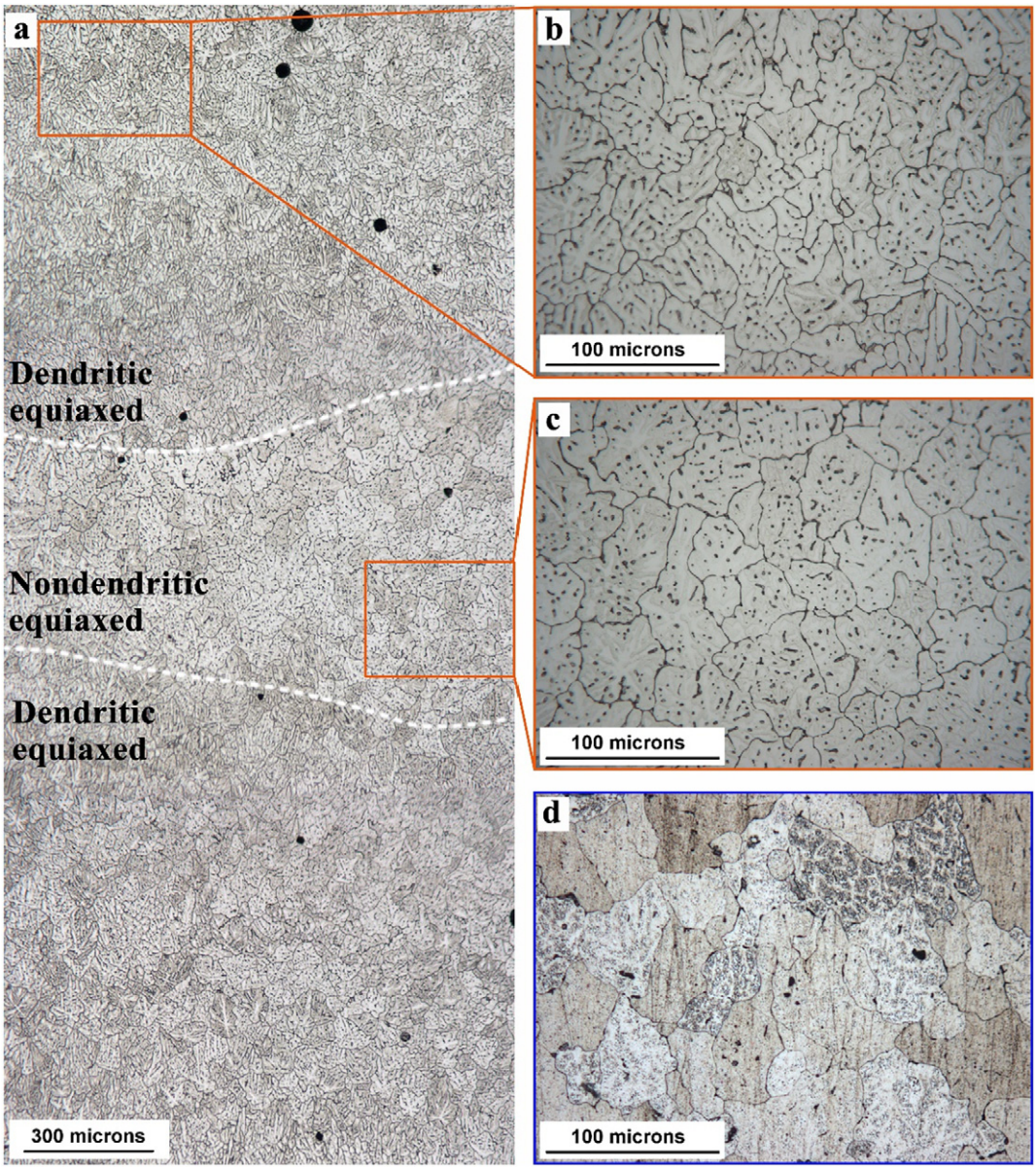

Fig. 3. Microstructure of as-deposited alloy; (a) overview metallograph; (b,c) magnification of enclosed regions in (a). (d) Microstructure of T6 heat-treated alloy.

grain distribution was not uniform throughout the cross-section of the as-deposited material, composing of dendrites, equiaxed grains, and a slight number of columnar grains. This distinct microstructure is similar to the as-deposited WAAM Al—Cu6.3 alloy [26] but different from conventional Al-Cu-Mg alloys manufactured by casting, rolling, or forging.

Fine dendrites and columnar grains developed above the fusion line by re-melting the topmost of each preceding layer. This is due to the larger temperature gradient generated at the bottom molten pool toward the previously solidified deposit [27]. Given the heat accumulation effect, heat dissipation continuously becomes slower with the decrease in a temperature gradient, approaching a thermal balance. Intra-layer grains grow spatially with the similar speed in each direction, thereby developing coarser equiaxed grains with dendrites away from the inter-layer boundary (fusion line). The average grain diameter of the upper enclosed region in Fig. 3a and b was about 16.8 μm by measuring with the IPP software. As shown in Fig. 3a and c, the inter-layer region within a height of 50–800 μm was characterized by equiaxed grains with a slight number of dendrites. The mean grain diameter was 17.5 μm in this inter-layer region, which located at the top of each solidified layer performing as the heat-affected zone. The few dendrites and slightly larger grains of the inter-layer zone were caused by the exposure to the thermal field of the subsequent molten droplet and the arc.

After the T6 heat treatment, the considerable number of dendritic grains in the as-deposited status was significantly diminished as shown in Fig. 3d. The mean grain size of the heat-treated alloy was coarsened by 10% reaching 18.9 μm. The driving force of the grain growth is due to the loss of equilibrium state between the thermodynamic growing and the pinning effect. Concerning the studied alloy, the miscellaneous sized second phase particles distributed in the matrix can impede the movement of the grain boundary. Along with the dissolution of phase particles under high temperature, the pinning effect is weakened accompanying grain expansion.

From the 3D view in Fig. 4a and b, the second phase particles (red) were network-like distributed in the as-deposited alloy with an average equivalent size of 2.8 μm. The micropores (blue) were surrounded by particle arms. Phase particles were not completely connected in the magnified Fig. 4b. Under high temperature of the molten droplet and arc, the partial melting of phase particles in the inter-layer equiaxed grain region leads to a disconnection between thin arms and an increase of phase spacing. Therefore, the number density of second phase particles in the inter-layer zone of the as-deposited alloy was increased by 17% compared with the intra-layer region from 1.04×10^6 to 1.22×10^6 per cubic millimeters. By contrast, the volume fraction of phase particles in the inter-layer region (19%) was 10% less than that of the intra-layer zone (21%). As shown in Fig. 4c, most of the particles disappeared, or became smaller and spherical, after the T6 heat treatment. Several residual particles as magnified in Fig. 4d had a similar morphology to the state before heat treatment. The number density of the particles was considerably decreased by 83% and 88% in the intra- and inter-layer regions. In other words, phase particles with a number density of 0.13×10^6 to 0.21×10^6 per cubic millimeters were undissolved in the heat-treated alloy. The volume fraction of particles in the heat-treated status, reducing by 95% in both regions, was 1% and 0.9% for the intra- and inter-layer regions, respectively.

Fig. 5 shows the SEM images of second phase particles on the 2D cross-section of the WAAM Al—Cu4.3—Mg1.5 alloys before and after heat treatment. Phase particles were mainly formed along grain boundaries of the as-deposited WAAM alloy as shown in Fig. 5a. After the heat

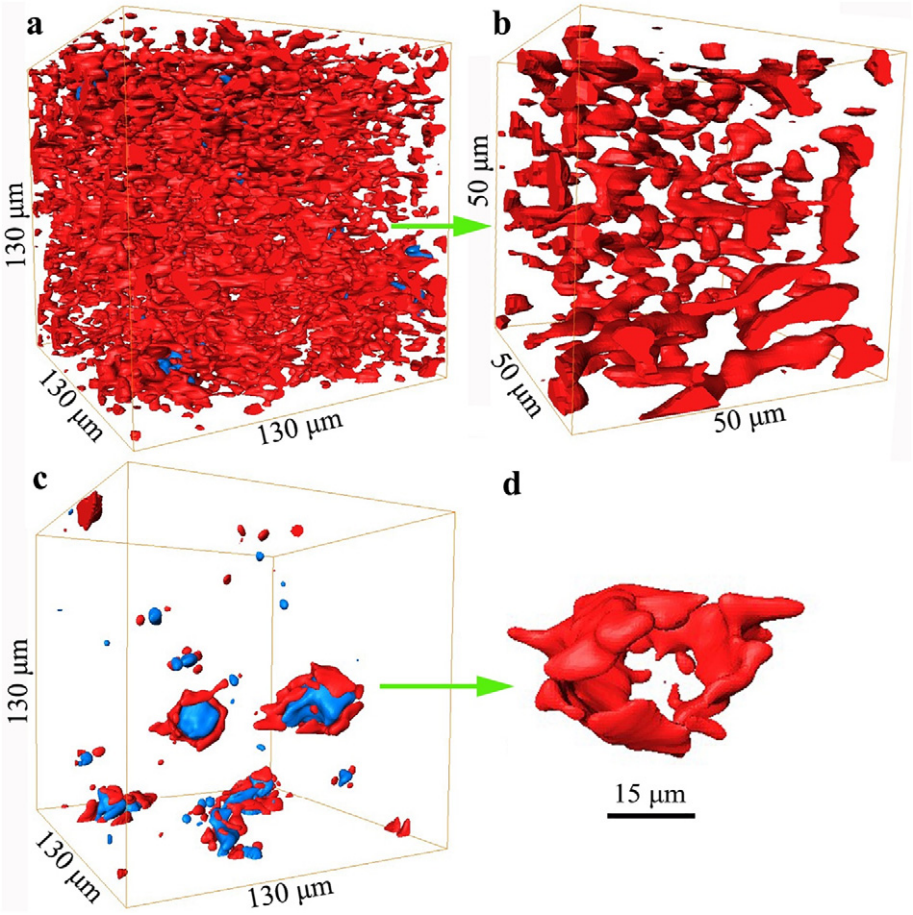

Fig. 4. 3D view of second phases (red) and micropores (blue) distribution; (a,b) as-deposited and (c,d) heat-treated; (b) and (d) magnification of phase particles in (a) and (c). (For interpretation of the references to color in this figure legend, the reader is referred to the web version of this article.)

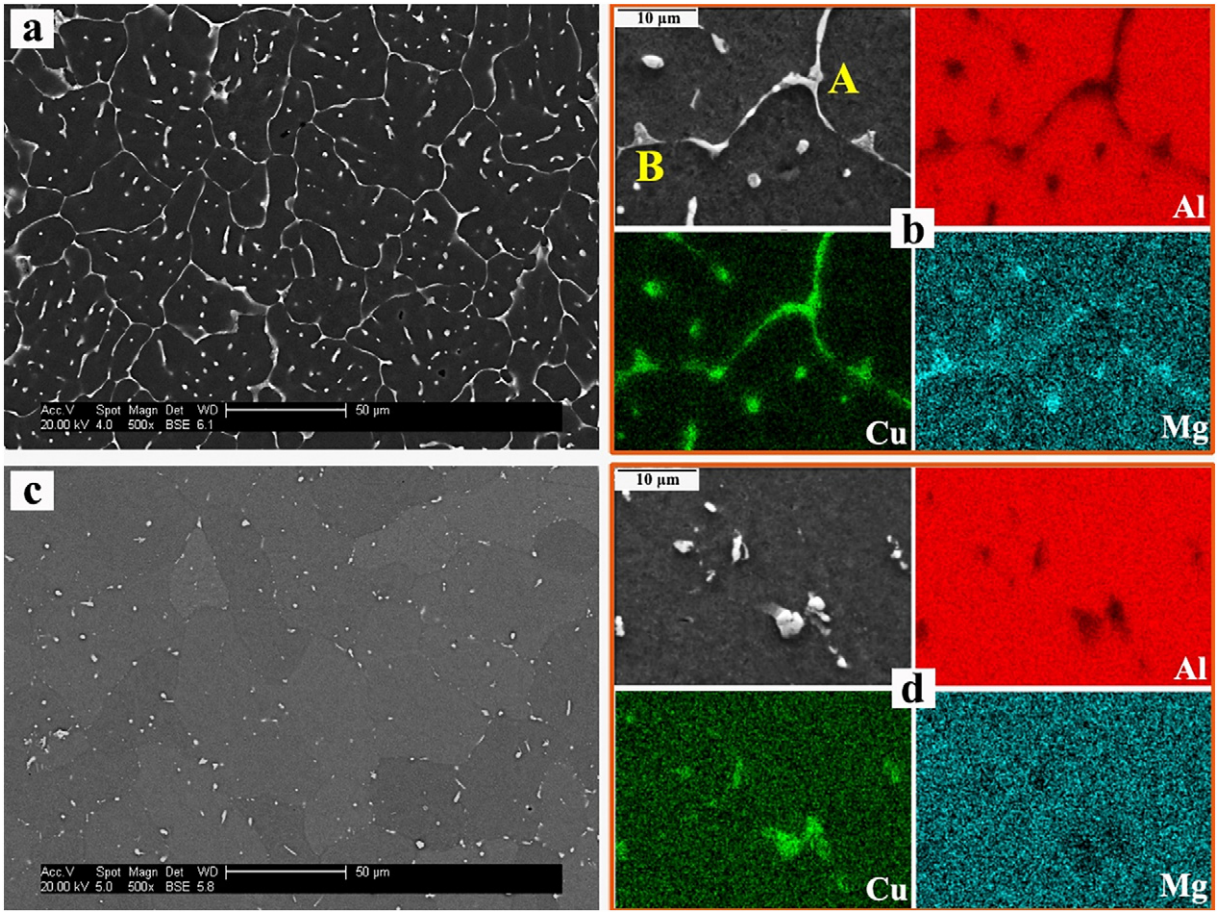

Fig. 5. SEM images of WAAM alloys; (a, b) as-deposited and (c, d) heat-treated, where (b) and (d) are map scanning of elements.

treatment, most of these grain boundary clustered particles were dissolved in the matrix during the solid solution due to elemental diffusion. The real spatial distribution of the in-homogeneously scattered particles is shown in Fig. 4c.

EDS analysis of element mapping is shown in Fig. 5b and d. The distinguished color indicates the location of the individual elements. The phase particles showed a eutectic morphology before heat treatment. The Cu element was seriously segregated along the grain boundaries. The Mg element was distributed more homogeneously in the α-Al matrix. The scatter of Mg on grain boundary exhibited a local concentration feature but this element was not found at the triple junction region. The EDS spot scanning revealed the composition of the bright white and dark white particles on the grey matrix in Fig. 5b was $Al_{62.36}Cu_{36.46}Mg_{1.18}$ and $Al_{71.24}Cu_{16.62}Mg_{12.14}$, respectively. The Cu-rich particle and Cu/Mg-rich particle in the ternary eutectic phases may be identified as θ phase and S phase, respectively. After the heat treatment in Fig. 5d, although the Cu element exhibited an increasingly homogeneous distribution, the undissolved white particles were identified as the θ phase but the S phase was not found. This is because the S phase can be near-completely dissolved under adequate solution treatment time. According to the phase diagram, the melting temperature of the θ phase reaches 548 °C. Therefore, several particles of the θ phase were retained in the matrix because of insufficient dissolution under the T6-temper condition in this study.

3.2. Defects in WAAM alloys

The spatial distribution and morphology of defects generated during solidification or after heat treatment were revealed by XRT. The reconstructed 3D images are shown in Fig. 6. Micropores or microvoids with miscellaneous sizes and morphology existed in the as-deposited (Fig. 6a) and heat-treated (Fig. 6b) WAAM Al—Cu4.3—Mg1.5 alloys. A defect-concentrated zone, the inter-layer region, was exhibited in the as-deposited WAAM alloy. Micropores tend to coalescent or float upward and to escape from the molten metal during solidification but may be hindered by dendritic arms and oxide films. Moreover, the arc and molten pool during the subsequent deposition may cause an increase and growth of micropores in the local area. A cluster of micropores with increasingly larger volume and number are eventually trapped at the top region of each deposited layer.

Typical individual micropore A-C were extracted from the as-deposited WAAM alloy. These micropores exhibited rough surface morphology. The micropore with a near-spherical shape like C is primarily formed by the entrapped hydrogen [28]. Sharp-angled defects like linear (A) and chain-like (B) cavities due to solidification shrinkage generally have negative impacts on the mechanical performance of WAAM aluminum components in yielding the bearing area [29]. After the heat treatment, micropores in the WAAM alloy coalesced (D), spheroidized (F), or stayed like that in the as-deposited state. The micropores number density and the characteristics of the size, volume, and roundness of each micropore were quantified and shown in Table 2.

The number density ρ refers to the pore numbers per unit volume of the alloy, while the volume fraction V_f is the micropore volume per unit volume of the alloy. The equivalent diameter d of each micropore was defined by Eq. (1). Sphericity S_p was defined in Eq. (2) as the ratio of the equivalent surface area of a spherical micropore to the measured surface area S of each actual pore [30],

$$d = 2\sqrt[3]{3V/4\pi}, \quad (1)$$

$$Sp = \sqrt[3]{36\pi V^2}/S, \quad (2)$$

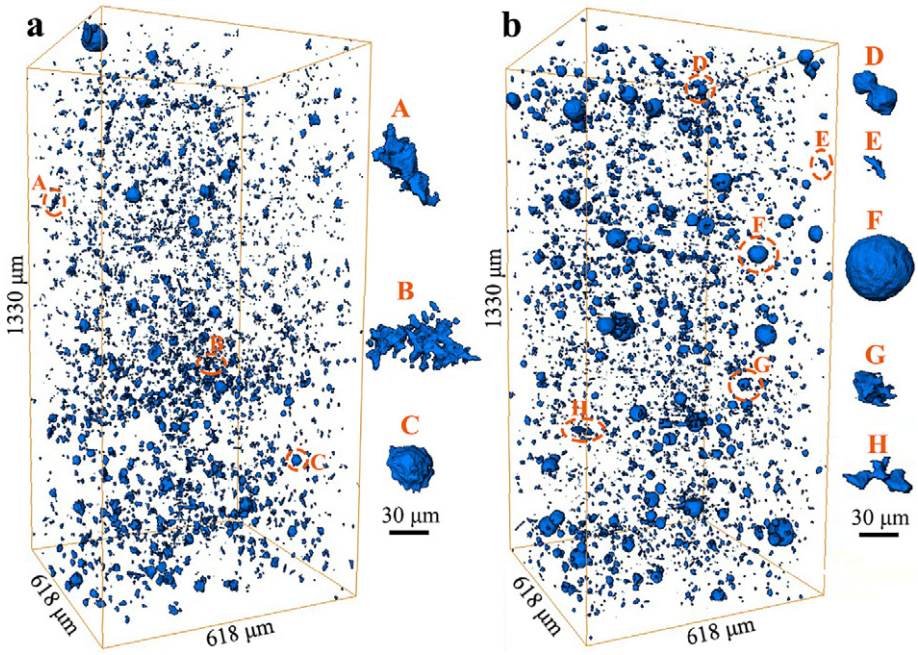

Fig. 6. 3D view of micropores in WAAM alloys; (a) as-deposited and (b) post-deposition T6 heat-treated.

where V and S are the reconstructed actual volume and surface area, respectively. For an ideal spherical pore, S_p is equal to 1. When S_p is relatively small, the 3D shape of a pore tends to be sheet-like, rod-shaped, or increasingly complicated.

Although a considerable number of micropores with a density of 15.4×10^3 per cubic millimeter existed in the as-deposited WAAM alloy, the volume density of this alloy reached 99.43%. After the heat treatment, the number density ρ of micropores reduced by 15%. By contrast, the average d, S_p, and V_f were increased by 9%, 7%, and 11%, respectively. The mean S_p of 0.74 in the heat-treated WAAM Al—Cu4.3—Mg1.5 alloy was identical to that in the annealed Al—Mg4 alloy as reported by Toda et al. [31].

Fig. 7a and b are the scattering plots of the micropore number fraction as a function of the equivalent diameter. Most micropores in the as-deposited and heat-treated WAAM alloys concentrated around 3.25–7.5 μm. After the heat treatment, the number of micropores >5 μm increased by 14% whilst the number of micropores <5 μm reduced by 20%, suggesting a volume growth of micropores. Fig. 7c and d plot the distribution of micropore number fractions by sorting their sphericity at an interval of 0.02. After the heat treatment, the peak value moved from around 0.75 in the as-deposited alloy toward 0.85 in the heat-treated alloy. The number of micropores with sphericity >0.7 increased by 46%. The above analysis suggested that Ostwald ripening [32] may be the dominant factor in charging of the micropore evolution, such as growth or agglomeration during the heat treatment. As shown in Fig. 4, micropores usually grow along with the network of eutectic particles resulting in large micropores with low sphericity in this alloy. After the heat treatment, most of the coarse micropores embedded between the phase particles as shown in Fig. 4c. A considerable number of phase interfaces between the micropore and matrix, micropore and particle, as well as particle and matrix will provide potential fracture-initiating sources, lowering the mechanical properties, especially in the vertical direction.

3.3. Mechanical properties of WAAM alloys

Microhardness test results in the vertical direction of the as-deposited and heat-treated alloy are shown in Fig. 8. The average microhardness value of 161.4 HV for the heat-treated alloy increased by 51% from 106.8 HV of the as-deposited alloy. With a fluctuation range between 156 and 166 HV, the microhardness became more homogeneously distributed after the heat treatment. A possible reason for the fluctuation of microhardness lays in the hierarchical scattering of grain morphology. Moreover, the microhardness may be weakened by the considerable number of defects like micropores in the WAAM alloy.

The bar graph in Fig. 9a shows the tensile properties of yield strength (YS), ultimate tensile strength (UTS), and elongation for the as-deposited and heat-treated WAAM Al—Cu4.3—Mg1.5 alloy. The mean YS, UTS, and elongation in the horizontal direction of the as-deposited alloy were 185 MPa, 293 MPa, and 12%, respectively. By contrast, although the YS stayed unchanged, the UTS and elongation in the vertical direction were 245 MPa and only 4%. After the T6 heat treatment, the YS and UTS in the horizontal direction increased by 116% and 66%, achieving 399 MPa and 485 MPa, respectively. The elongation was decreased to 9%. These values are close to the properties of the conventional wrought 2024-T6 aluminum alloy, the YS, UTS, and elongation of which were 393 MPa, 476 MPa and 10% at room temperature [33]. Compared with the horizontal properties, the vertical elongation of the heat-treated alloy was only around 2% accompanying with an 11% reduction of the mean UTS value, which was 430 MPa. The vertical YS was 4%

Table 2
Quantitative analysis of micropores in as-deposited and heat-treated WAAM Al—Cu4.3—Mg1.5 alloys.

Alloy status	Micropore			
	Number density ρ (10^3/mm^3)	Average equivalent diameter d (μm)	Volume fraction V_f (%)	Average sphericity S_p
As-deposited	15.4	6.9	0.57	0.69
Heat-treated	13.1	7.5	0.63	0.74

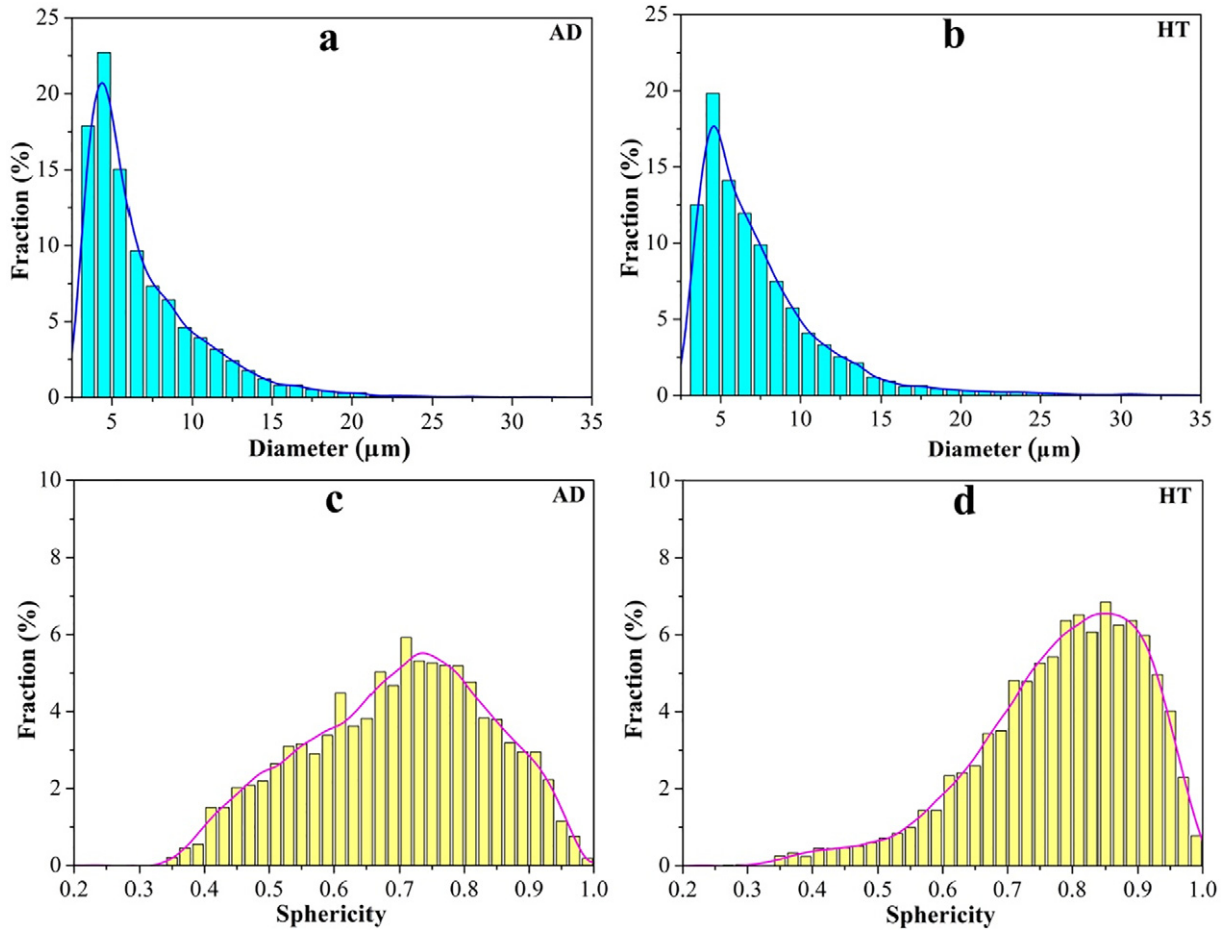

Fig. 7. Micropore number fraction in WAAM alloys as a function of (a, b) equivalent diameter and (c, d) sphericity, where (a, c) and (b, d) are as-deposited and heat-treated, respectively.

lower than that of the horizontal value. The strength and plasticity measured from the two directions yielded non-uniform values, indicating that the mechanical properties are directionally dependent for the WAAM Al—Cu4.3—Mg1.5 alloy.

Fig. 9b shows the engineering stress-strain curves of the WAAM alloy before and after the T6 heat treatment. All the tested alloys did not have obvious yielding points during the tensile test. The slopes of the linearly elastic deformation were almost the same for the as-deposited and the T6 heat-treated WAAM specimens in both directions. The strengthening effect of dynamic strain aging, normally revealed by the serrated patterns, was not found in these WAAM alloys. A similar tensile trend existed in both directions. The difference between the two directions was that the vertical specimen was suddenly fractured before reaching its limit strength as exhibited in the horizontal direction.

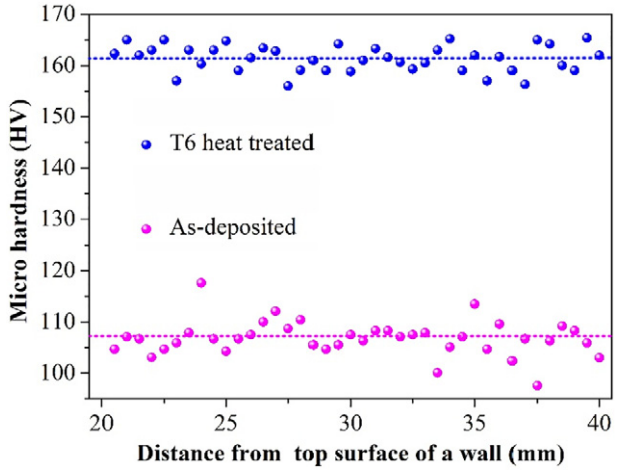

Fig. 8. Microhardness distribution in as-deposited and heat-treated WAAM alloys.

3.4. Strengthening and fracturing mechanisms

Fig. 10 shows the bright-field TEM images taken from the middle region of the as-deposited and heat-treated walls of the WAAM Al—Cu4.3—Mg1.5 alloy. Dislocations and rod-shaped orthorhombic T ($Al_{20}Cu_2Mn_3$) phases [34] with a typical length of 80–400 nm and an aspect ratio ranging from 2 to 6 were observed in the as-deposited WAAM alloy (Fig. 10a). The presence of the fine T phase generally causes dislocation tangling under plastic deformation [35]. This is the main reason for the higher strength of the as-deposited WAAM Al—Cu4.3—Mg1.5 alloy than the WAAM Al—Cu6.3 alloy, which has only coarse θ phases in the as-deposited matrix [15]. As shown in Fig. 10b, the microstructure of the heat-treated WAAM Al—Cu4.3—Mg1.5 alloy was characterized by a high density of needle-shaped metastable S′ precipitates [35,36] and few T phases. The precipitation of the considerable number of metastable phases with a parallel or perpendicular relationship, up to 1 μm in length, accounts for the remarkable increase of microhardness and strength after heat treatment by resisting dislocation slip and trapping dislocations.

The anisotropic tensile properties of WAAM alloys can be revealed from the side views of the fractured tensile samples in Fig. 11. Each layer of the horizontal sample was parallel with the force direction. The fracture line propagated across all the layers as shown in the side

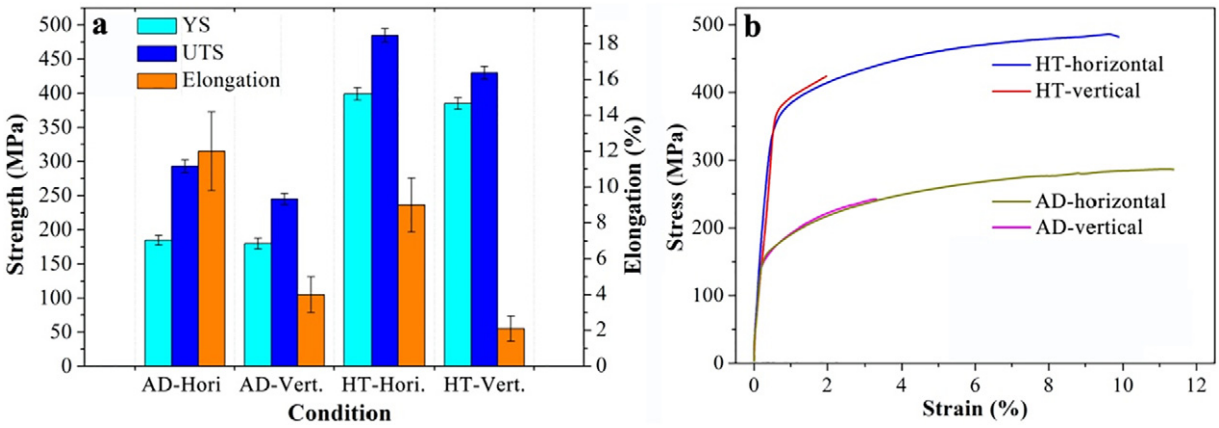

Fig. 9. Tensile properties of as-deposited and heat-treated WAAM alloys; (a) mean values of YS, UTS, and elongation; (b) stress-strain curves.

view of Fig. 11a. Comparatively, the inter-layer boundaries of the vertical sample were perpendicular to the tensile load. This sample fractured along with the inter-layer boundary in Fig. 11b. As discussed in Section 3.2, the inter-layer region is generally concentrated with defects. This could be revealed by the comparison between the striped concentration (Fig. 11a) and homogeneous distribution (Fig. 11b) of micro-pore/crack on the fracture surface of the horizontal and vertical samples, respectively. Therefore, cracks easily propagated along this region due to its smaller loading area and lower bearing capacity when the tensile load was brought in the vertical direction.

The metallographs of the fractured WAAM Al—Cu4.3—Mg1.5 alloy in both directions are shown in Fig. 12. The microstructure exhibited a similar feature at each side of the fracture line in Fig. 12a, suggesting that the tensile properties in the horizontal direction of the as-deposited alloy are independent of its inhomogeneous microstructure. Microcracks parallel to the fracture line may be initiated from the inter-granular defects like micropore as marked by the upper right arrow in Fig. 12a. From the SEM observation in Fig. 13a, these parallel cracks performed on the horizontally fractured surface. Several microcracks perpendicular to the fracture line as shown in Fig. 12a neighbored to the inter-layer boundary. Microracks parallel with the fracture line of the vertical sample (Fig. 12b) act as cracking initiation source and propagation site under the tensile load. The fracture line in Fig. 12b separating dendritic grains from pure equiaxed grains was the inter-layer boundary. Therefore, the interfaces of overlapping melted tracks act as metallurgical weaknesses, giving rise to the inferior plasticity in the vertical direction. The considerable number of microcracks from the SEM fractographic morphology in Fig. 13b verified the brittle fracture characteristic at the inter-layer boundary of the vertically fractured alloy.

The fractured profile of the heat-treated tensile sample along the horizontal direction is shown in Fig. 12c, exhibiting the same grain morphology at each fractured side. The micropores and microcracks were marked out as well. The fracture line of the vertically fractured heat-treated alloy in Fig. 12d separated equiaxed grains from small equiaxed and columnar grains, which is the sign of inter-layer boundary as shown in Fig. 3. In a word, the fracture characteristics of each direction for the heat-treated WAAM Al—Cu4.3—Mg1.5 alloy are similar to that of the as-deposited alloy.

Fig. 13 exhibits the SEM images of the fractured surface in both directions. Several coarse dimples with sizes from 5 to 18 μm, the sign of ductile fracture, were shown on the horizontally fractured surface of the as-deposited alloy in Fig. 13a. The inner surface of each dimple in the magnified image was covered by pieces of fragment, revealing that brittle fracture contributed to the failure as well. Except solidification microcracks, the upper arrow pointing tear suggested that microcracks could also initiate from the fractured coarse particles and their phase interfaces. By contrast, the number of dimples decreased, but the number of micropores increased for the vertical fracture surface in Fig. 13b. The solidification cracks on this surface is responsible for the rupture along the vertical direction, exhibiting a brittle fracture mode.

Most of the fracture surface of the heat-treated alloy (Fig. 13c and d) was taken by smaller and shallower dimples, as demonstrated in the magnified image in Fig. 13c, suggesting a ductile fracture with high strength. Although cleavage planes or cleavage steps were not obvious on the fracture surface of the heat-treated alloys, solidification cracks were inherited from the as-deposited alloy. The cracks located on the inter-layer boundary as shown in Fig. 13d caused a low elongation of 2% for the vertically fractured specimen. These cracks may be developed by the inter-grain defects or from the fractured brittle phase particles (Fig. 13d). EDS analysis revealed the composition of the cracked particle was $Al_{67.32}Cu_{32.68}$, which was the undissolved θ phase.

In conclusion, all four fractured surfaces were characterized by both inter- and intra-gain fracture. The ductile fracture mode may dominate

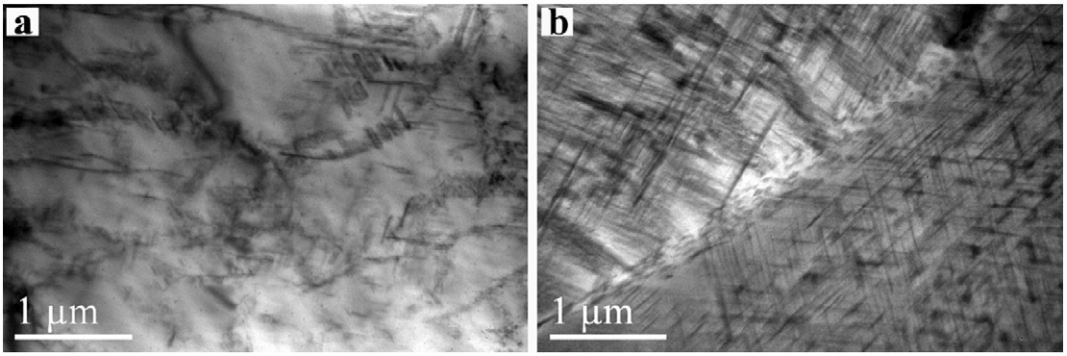

Fig. 10. TEM images of WAAM Al—Cu4.3—Mg1.5 alloys; (a) as-deposited and (b) after-deposition T6 heat-treated.

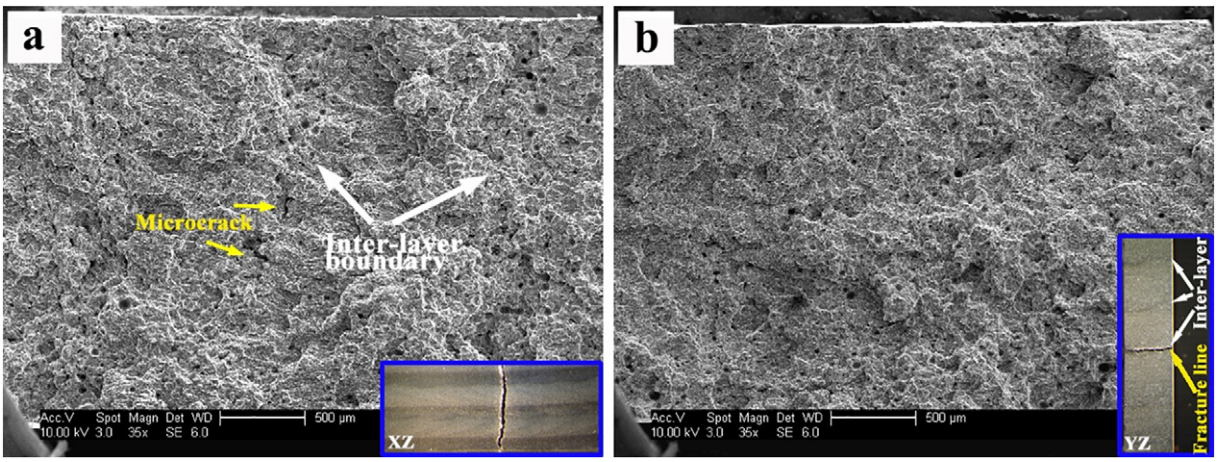

Fig. 11. Side-view and fractographic morphology of fractured tensile samples for as-deposited alloy with loading direction in (a) horizontal and (b) vertical.

the horizontal fracture for both the as-deposited and heat-treated WAAM alloys. By contrast, the low YS and elongation properties of the vertically fractured WAAM alloy suggested that the brittle fracture may be the main reason for the failure in this direction.

3.5. Development of WAAM aluminum alloys

Tensile properties along the horizontal direction of WAAM aluminum alloys in literatures and this work were summarized in Fig. 14. The strength of the Al—Cu4.3—Mg1.5 alloy in this work ranks as the highest among all the referenced as-deposited alloy, whilst the elongation of this alloy stays at a medium level. Solid solution strengthening dominates the relatively higher strength of the ternary Al-Cu-Mg alloys and binary Al—Mg alloys. Although the strength of WAAM alloys, either heat-treatable or non-heat treatable, could be remarkably improved by using hybrid WAAM manufacturing techniques like inter-layer rolling [15], laser shock peening [37], or workpiece vibration [14], the elongation generally decreased with increasing forces. In addition, the application of hybrid method may rise the flexibility of plant and lower the forming efficiency.

Post-deposition heat treatment is an effective method in promoting mechanical properties of aluminum alloys on the basis of precipitation strengthening. Only aluminum alloys belonging to 2000, 6000, 7000 series can be heat treatment strengthened. However, the performance of WAAM Al-Si-Mg or Al-Zn(-Mg-Cu) alloys has seldom been published due to the short supply of the corresponding wires. The strength of the alloy in this work, especially the yield strength, is relatively higher than that of the heat-treated WAAM 2319 [15] and 2024 [25] alloys. Although the composition of the Al—Cu4.3—Mg1.5 alloy in this work is similar to that of the 2024 alloy manufactured by Qi et al. [25], the

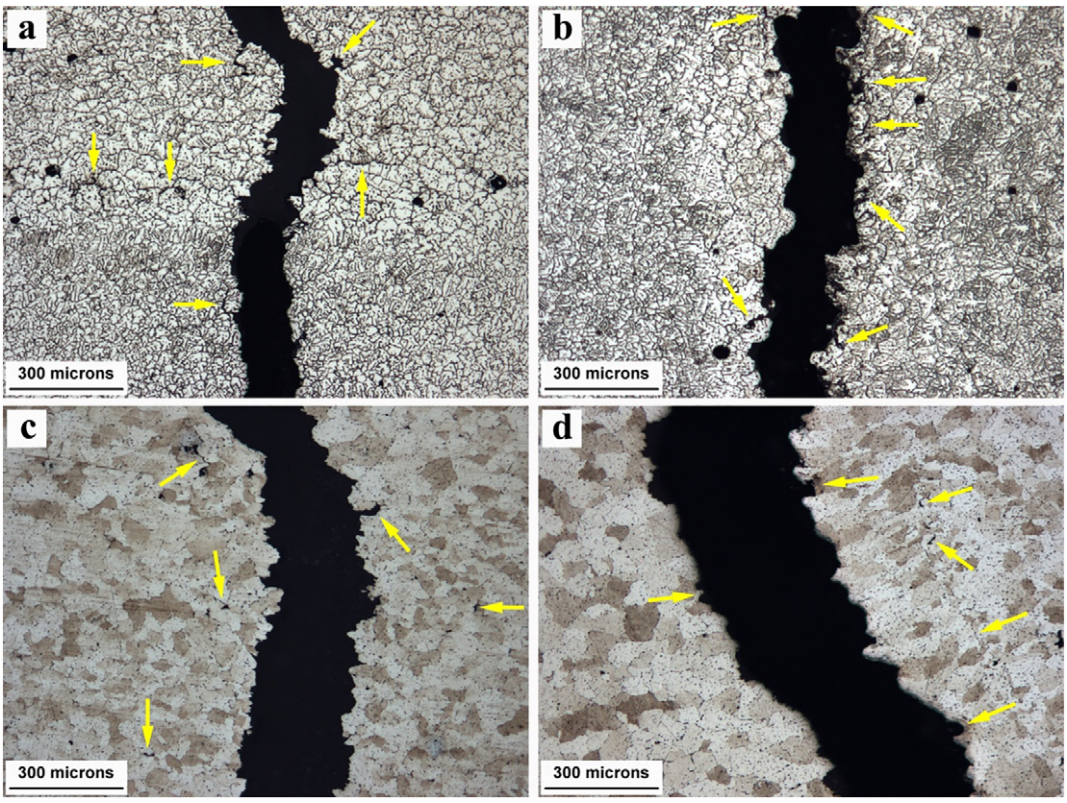

Fig. 12. Metallographs of the fractured position of WAAM alloys; (a, b) as-deposited and (c, d) after-deposition T6 treated, where (a, c) and (b, d) are in horizontal and vertical directions, respectively.

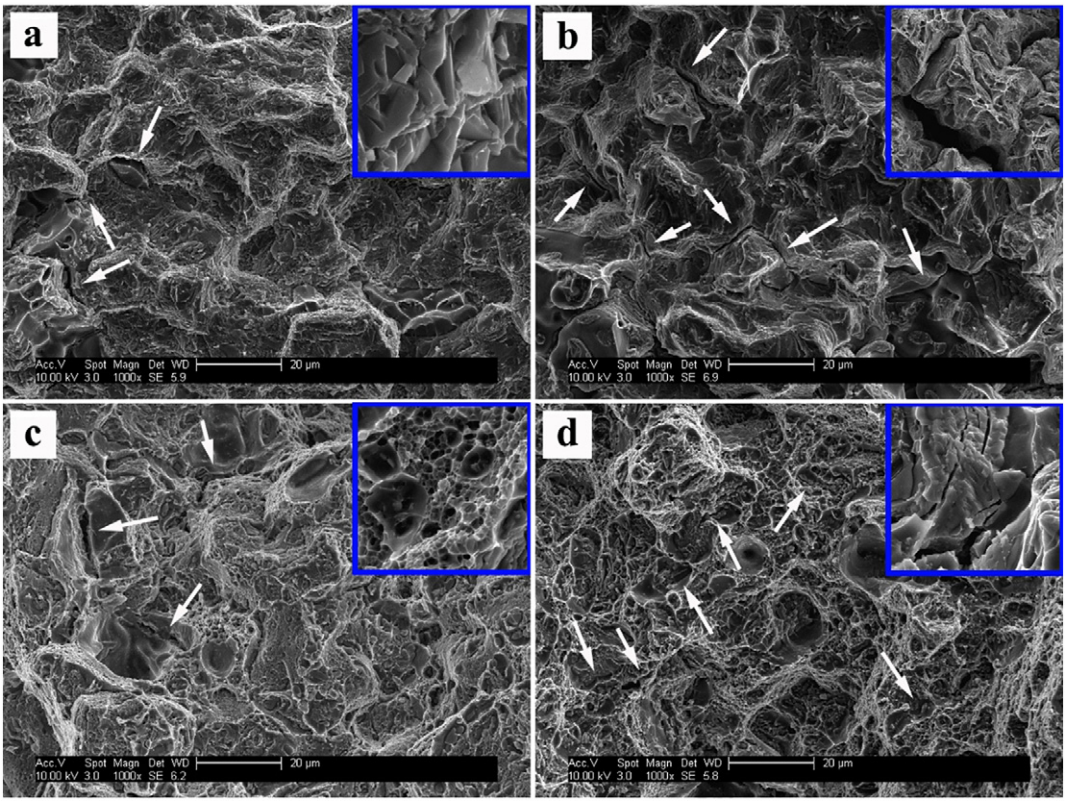

Fig. 13. SEM fractographic morphology for tensile samples of WAAM alloys; (a, b) as-deposited and (c, d) after-deposition T6 treated, where (a, c) and (b, d) are in horizontal and vertical directions, respectively.

strength of the tandem built 2024 alloy may be lowered due to its high deposition heat input.

Many problems still need to be solved for the WAAM alloy in this study. First, in optimizing mechanical properties, the overall exposure time during the heat treatment must be deliberately considered to realize a complete dissolution of particles while suppressing micropores ripening, microvoids formation, and grain growth [40]. Second, the composition of the dedicated filler material should be optimized to realize an isotropy property for the WAAM alloy, for example, adding grain refiners like Ti as reported by Wang et al. [18]. Last, the hybrid WAAM technique like inter-layer rolling [15] or peening [37] may be an effective way in eliminating defects and improving vertical properties.

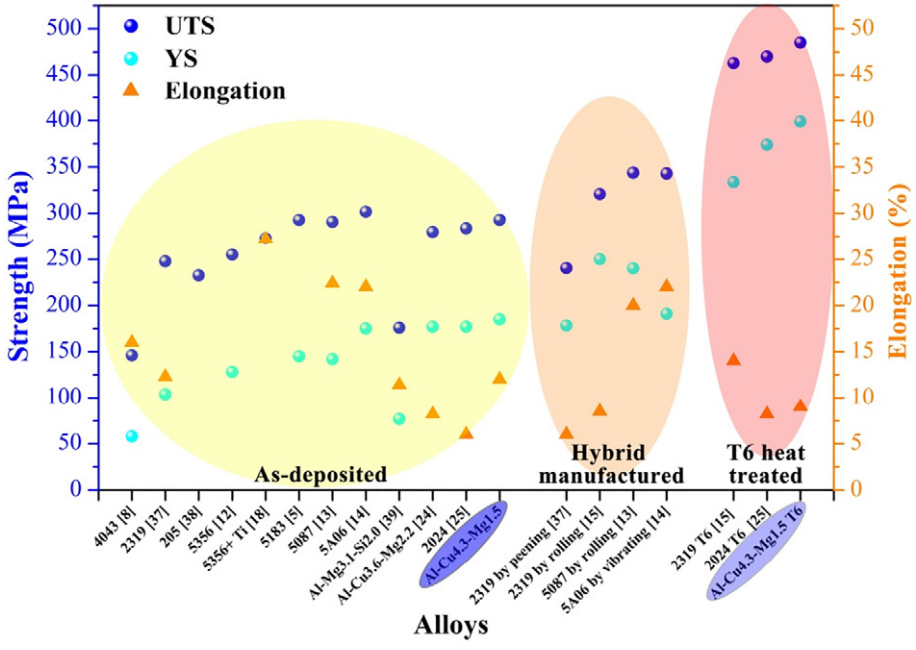

Fig. 14. Tensile properties of WAAM aluminum alloys in this work and Refs. [5, 8, 12–15, 18, 24, 25, 37–39].

4. Conclusions

The WAAM Al—Cu4.3—Mg1.5 alloy was manufactured by using a single feeding wire and the traditional CMT-WAAM deposition system. The microstructure and mechanical properties of the as-deposited and heat-treated WAAM alloys were studied. Key findings are drawn as follows:

(1) The microstructure of the as-deposited alloy was characterized by a hierarchical distribution of dendrites, equiaxed grains, and a slight number of columnar grains. Second phase particles with a volume fraction of 19%–21% scattered network-like along grain boundaries. After the T6 heat treatment, most $\alpha + \theta + S$ eutectics were dissolved, leaving a volume fraction of 0.9%–1% of the θ phase.
(2) As revealed by XRT, a considerable number of sharp-angled defects like linear and chain-like micropores or microcavities were formed in the WAAM alloys. The 15% reduction in number density, and 9%, 7%, 11% increase in average diameter, average sphericity, and volume fraction of micropores suggested that Ostwald ripening may dominate the micropore evolution after heat treatment.
(3) After heat treatment, the average microhardness of 161.4 HV was increased by 51% from the as-deposited alloy. With an elongation of 9%, the mean YS and UTS increased by 116% and 66% achieving 399 MPa and 485 MPa in the horizontal direction. The mechanical properties of the heat-treated alloy were enhanced by precipitation strengthening due to the high density of needle-shaped metastable S′ precipitates.
(4) The lower YS and elongation in the vertical direction suggested an anisotropic property of the WAAM alloy. The tensile failure in the horizontal and vertical directions was dominated by the ductile fracture and brittle fracture, respectively. The inter-layer boundary acts as metallurgical weaknesses for this WAAM alloy.

CRediT authorship contribution statement

Jianglong Gu: Data curation, Formal analysis.**Minjie Gao:** Investigation.**Shouliang Yang:** Investigation.**Jing Bai:** Methodology, Supervision. **Yuchun Zhai:** Methodology, Writing - review & editing.**Jialuo Ding:** Methodology, Writing - review & editing.

Declaration of competing interest

The authors declare that they have no known competing financial interests or personal relationships that could have appeared to influence the work reported in this paper.

Acknowledgements

This work was supported by Natural Science Foundation of Hebei Province (E2019203364). Thanks also go to NEIMM in China for their supply of wires and Shanghai Synchrotron Radiation Facility for their help in testing with the beamline BL13W1.

Data availability

The raw/processed data required to reproduce these findings cannot be shared at this time as the data also forms part of an ongoing study.

References

[1] T. Debroy, H. Wei, J. Zuback, T. Mukherjee, W. Zhang, Additive manufacturing of metallic components-process, structure and properties, Prog. Mater. Sci. 92 (2018) 112–224.
[2] B.T. Wu, Z.X. Pan, D.H. Ding, D. Cuiuri, H.J. Li, J. Xu, J. Norrish, A review of the wire arc additive manufacturing of metals: properties, defects and quality improvement, J. Manuf. Process. Technol. 35 (2018) 127–139.
[3] S.W. Williams, F. Martina, A.C. Addison, J.L. Ding, G. Pardal, P.A. Colegrove, Wire + arc additive manufacturing, Mater. Sci. Technol. 32 (2015) 641–647.
[4] K.S. Derekar, A review of wire arc additive manufacturing and advances in wire arc additive manufacturing of aluminium, Mater. Sci. Technol. 34 (2018) 1–22.
[5] A. Horgar, H. Fostervoll, B. Nyhus, X. Ren, M. Eriksson, O.M. Akselsen, Additive manufacturing using WAAM with AA5183 wire, J. Mater. Process. Technol. 259 (2018) 68–74.
[6] K.F. Ayarkwa, S.W. Williams, J. Ding, Assessing the effect of TIG alternating current time cycle on aluminium wire + arc additive manufacture, Addit. Manuf. 18 (2017) 186–193.
[7] J.P. Oliveira, T.G. Santos, R.M. Miranda, Revisiting fundamental welding concepts to improve additive manufacturing: from theory to practice, Prog. Mater. Sci. (2019) 100590, https://doi.org/10.1016/j.pmatsci.2019.100590.
[8] D. Wang, J. Lu, S. Tang, L. Yu, H. Fan, L. Ji, C. Liu, Reducing porosity and refining grains for arc additive manufacturing aluminum alloy by adjusting arc pulse frequency and current, Mater 11 (2018) 1344 1–14.
[9] J.L. Gu, B.Q. Cong, J.L. Ding, S.W. Williams, Y.C. Zhai, Wire + arc additive manufacturing of aluminium, Proceedings of the 25th Annual International Solid Freeform Fabrication Symposium 2014, pp. 451–458.
[10] J.Y. Bai, C.L. Yang, S.B. Lin, B.L. Dong, C.L. Fan, Mechanical properties of 2219-Al components produced by additive manufacturing with TIG, Int. J. Adv. Manuf. Technol. 86 (2016) 479–485.
[11] M.S. Domack, K.M. Taminger, M. Begley, Metallurgical mechanisms controlling mechanical properties of aluminium alloy 2219 produced by electron beam freeform fabrication, Mater. Sci. Forum 519-521 (2006) 1291–1296.
[12] C.C. Su, X.Z. Chen, C. Gao, Y.F. Wang, Effect of heat input on microstructure and mechanical properties of Al-Mg alloys fabricated by WAAM, Appl. Surf. Sci. 486 (2019) 431–440.
[13] J. Gu, X. Wang, J. Bai, J. Ding, S. Williams, Y. Zhai, Deformation microstructures and strengthening mechanisms for the wire + arc additively manufactured Al-Mg4.5Mn alloy with inter-layer rolling, Mater. Sci. Eng. A 712 (2018) 292–301.
[14] C. Zhang, M. Gao, X. Zeng, Workpiece vibration augmented wire arc additive manufacturing of high strength aluminum alloy, J. Mater. Process. Technol. 271 (2019) 85–92.
[15] J. Gu, J. Ding, S. Williams, H. Gu, J. Bai, Y. Zhai, P. Ma, The strengthening effect of inter-layer cold working and post-deposition heat treatment on the additively manufactured Al-6.3Cu alloy, Mater. Sci. Eng. A 651 (2016) 18–26.
[16] X. Nie, H. Zhang, H. Zhu, Z. Hu, L. Ke, Effect of Zr content on formability, microstructure and mechanical properties of selective laser melted Zr modified Al- 4.24Cu-1.97Mg-0.56Mn alloys, J. Alloys Compd. 764 (2018) 977–986.
[17] J.H. Martin, B.D. Yahata, J.M. Hundley, J.A. Mayer, T.A. Schaedler, 3D printing of high-strength aluminium alloys, Nature 549 (2017) 365–369.
[18] L. Wang, Y. Suo, Z. Liang, D. Wang, Q. Wang, Effect of titanium powder on microstructure and mechanical properties of wire + arc additively manufactured Al-Mg alloy, Mater. Lett. 241 (2019) 231–234.
[19] E.A. Starke Jr., J. Staley, Application of modern aluminum alloys to aircraft, Prog. Aerosp. Sci. 32 (1996) 131–172.
[20] J. Liu, S. Kou, Susceptibility of ternary aluminum alloys to cracking during solidification, Acta Mater. 125 (2017) 513–523.
[21] J. Liu, S. Yang, S. Wang, J. Chen, C. Wu, The influence of Cu/Mg atomic ratios on precipitation scenarios and mechanical properties of Al-Cu-Mg alloys, J. Alloy. Compd. 613 (2014) 139–142.
[22] J.L. Gu, B. Jing, J.L. Ding, S. Williams, L.M. Wang, K. Liu, Design and cracking susceptibility of additively manufactured Al-Cu-Mg alloys with tandem wires and pulsed arc, J. Mater. Process. Technol. 262 (2018) 210–220.
[23] C.G. Pickin, S.W. Williams, P.B. Prangnell, J. Robson, M. Lunt, Control of weld composition when welding high strength aluminum alloy using the tandem process, Sci. Technol. Weld. Join. 14 (2009) 734–739.
[24] Z. Qi, B. Cong, B. Qi, H. Sun, G. Zhao, J. Ding, Microstructure and mechanical properties of double-wire + arc additively manufactured Al-Cu-Mg alloys, J. Mater. Process. Technol. 255 (2018) 347–353.
[25] Z. Qi, B. Qi, B. Cong, H. Sun, G. Zhao, J. Ding, Microstructure and mechanical properties of wire + arc additively manufactured 2024 Al alloy components: as-deposited and post heat-treated, J. Manuf. Process. 40 (2019) 27–36.
[26] X. Fang, L. Zhang, H. Li, C. Li, K. Huang, B. Lu, Microstructure evolution and mechanical behavior of 2219 aluminum alloys additively fabricated by the cold metal transfer, Mater. 11 (2018) 812–824.
[27] H.L. Wei, J.W. Elmer, T. Debroy, Origin of grain orientation during solidification of an Al alloy, Acta Mater. 115 (2016) 123–131.
[28] S.G. Lee, A.M. Gokhale, Formation of gas induced shrinkage porosity in Mg-alloy high-pressure die-castings, Scr. Mater. 55 (2006) 387–390.
[29] B.Q. Cong, J.L. Ding, S.W. Williams, Effect of arc mode in cold metal transfer process on porosity of additively manufactured Al-6.3%Cu alloy, Int. J. Adv. Manuf. Technol. 76 (2015) 1593–1606.
[30] J.S. Wang, P.D. Lee, Simulating tortuous 3D morphology of microporosity formed during solidification of Al-Si-Cu alloys, Int. J. Cast. Metal. Res. 20 (2007) 151–158.
[31] H. Toda, K. Minami, K. Koyama, K. Ichitani, M. Kobayashi, K. Uesugi, Y. Suzuki, Healing behavior of preexisting hydrogen micropores in aluminum alloys during plastic deformation, Acta Mater. 57 (2009) 4391–4403.
[32] H. Toda, T. Hidaka, M. Kobayashi, K. Uesugi, A. Takeuchi, K. Horikawa, Growth behavior of hydrogen micropores in aluminum alloys during high-temperature exposure, Acta Mater. 57 (2009) 2277–2290.
[33] J.R. Davis, Aluminum and Aluminum Alloys, ASM international, Ohio, 1993.
[34] Z. Zhang, B.L. Xiao, Z.Y. Ma, Hardness recovery mechanism in the heat-affected zone during long-term natural aging and its influence on the mechanical properties and

fracture behavior of friction stir welded 2024Al-T351 joints, Acta Mater. 73 (2014) 227–239.
[35] S. Cheng, Y. Zhao, Y. Zhu, E. Ma, Optimizing the strength and ductility of fine structured 2024 Al alloy by nano-precipitation, Acta Mater. 55 (2007) 5822–5832.
[36] D. Doppalapudi, P. Venkatachalam, S.R. Kumar, B. Ravisankar, K. Jayashankar, Improving the mechanical properties of 2024 Al alloy by cryo rolling, Trans. Indian Ins. Metal. 63 (2010) 31–34.
[37] R. Sun, L. Li, Y. Zhu, W. Guo, P. Peng, B. Cong, J. Sun, Z. Che, B. Li, C. Guo, L. Liu, Microstructure, residual stress and tensile properties control of wire-arc additive manufactured 2319 aluminum alloy with laser shock peening, J. Alloys Compd. 747 (2018) 255–265.
[38] T. Ma, J. Ge, Y. Chen, T. Jin, Y. Lei, Observation of in-situ tensile wire-arc additively manufactured 205A aluminum part: 3d pore characteristics and microstructural evolution, Mater. Lett. 237 (2019) 266–269.
[39] Z. Qi, B. Q, B. C, R. Zhang, Microstructure and mechanical properties of wire + arc additively manufactured Al-Mg-Si aluminum alloy, Mater. Lett. 233 (2018) 348–350.
[40] J. Gu, M. Gao, S. Yang, J. Bai, J. Ding, X. Fang, Pore formation and evolution in wire + arc additively manufactured 2319 Al alloy, Addit. Manuf. 30 (2019) https://doi.org/10.1016/j.addma.2019.100900.

2019-11-13

Microstructure, defects, and mechanical þÿ p r o p e r t i e s o f w i r e / + / a r c a d d i t manufactured AlCu4.3-Mg1.5 alloy

Gu, Jianglong

Elsevier

Gu J, Gao M, Yang S, et al., (2020) Microstructure, defects, and mechanical properties of þÿ w i r e / + / a r c a d d i t i v e l y m a n u f a c t u r e d A l C u 4 . 3 - M g 1 . 5 a l l o y . M a t e r i a l s a n d D January 2020, Article number 108357

https://doi.org/10.1016/j.matdes.2019.108357